Journal of Solid State Electrochemistry (2021) 25:45–56
https://doi.org/10.1007/s10008-019-04436-w

ORIGINAL PAPER

Oxygen reduction reaction mechanism and kinetics on M-N_xC_y and M@N-C active sites present in model M-N-C catalysts under alkaline and acidic conditions

Ricardo Sgarbi[1,2] · Kavita Kumar[2] · Frédéric Jaouen[3] · Andrea Zitolo[4] · Edson A. Ticianelli[1] · Frédéric Maillard[2]

Received: 6 August 2019 / Revised: 25 October 2019 / Accepted: 25 October 2019 / Published online: 16 November 2019

Abstract

M-N-C electrocatalysts (where M is Fe or Co) have been investigated for mitigating the dependence on noble metals when catalyzing the oxygen reduction reaction (ORR) for fuel cell technologies in acidic or alkaline conditions. Rotating disk and rotating ring-disk electrode measurements for Fe-N-C and Co-N-C catalysts demonstrate promising performances and stability for the ORR, while the activity of main suspected active sites (M-N_xC_y and M@N-C) has been discussed on the basis of the known physical-chemical properties of the catalysts in acid and alkaline media. Thereupon, it is observed that atomically dispersed Fe-N_xC_y sites reach the highest ORR activity in acid media when amplified by an adequate energy binding between the metallic center and the oxygenated reaction intermediates. In contrast, Fe@N-C core-shell sites reach a maximum ORR mass activity in alkaline media through a synergistic effect involving catalyst particles with metallic iron in the core and nitrogen-doped carbon in the shell.

Keywords Fe-N-C catalyst · Co-N-C catalyst · PGM-free catalysts · Alkaline exchange membrane fuel cell · Proton exchange membrane fuel cell

Introduction

The oxygen reduction reaction (ORR) electrocatalysis plays a key role in the development of sustainable and clean energy technologies, particularly when related to energy storage and conversion devices. Among these devices, fuel cells that convert the chemical energy of a fuel into electricity rely on air-reducing cathodes. Depending on the choice of electrolyte, fuel cells are operated in a broad range of pH, from acidic to neutral and alkaline conditions, as represented by the proton exchange membrane (PEMFC) and microbial (MFC) and alkaline exchange membrane (AEMFC) fuel cells, respectively [1, 2]. Catalysts based on platinum (Pt) and platinum-group metals (PGM) reach high activity and selectivity for ORR to water in acidic conditions [3], in the same way as several PGM catalysts exhibit good performances for ORR, with relative tolerance to fuel contamination, in alkaline media [4]. However, the high cost and the CO poisoning of PGM-based catalysts have been pointed out as unsolved problems for the wide-scale implementation of these devices [2, 5, 6].

Two classes of PGM-free catalysts have been widely investigated focusing on eliminating PGM for the ORR electrocatalysis: (i) metal-free carbon-nitrogen (N-C)

Dedicated to Professor José H. Zagal in celebration of his 70th birthday and his inspiring work on the reactivity of metal-macrocycles for O_2 electro-reduction and how this can apply to pyrolyzed Metal-N-C catalysts

Electronic supplementary material The online version of this article (https://doi.org/10.1007/s10008-019-04436-w) contains supplementary material, which is available to authorized users.

✉ Frédéric Jaouen
frederic.jaouen@umontpellier.fr

✉ Frédéric Maillard
frederic.maillard@lepmi.grenoble-inp.fr

[1] Instituto de Química de São Carlos, Universidade de São Paulo, Sao Carlos, SP 13560-960, Brazil

[2] Univ. Grenoble Alpes, Univ. Savoie Mont Blanc, CNRS, Grenoble INP, LEPMI, 38000 Grenoble, France

[3] CNRS, Université de Montpellier, ENSCM, UMR 5253 Institut Charles Gerhardt Montpellier, 2 place Eugène Bataillon, F-34095 Montpellier, France

[4] Synchrotron SOLEIL, L'orme des Merisiers, BP 48 Saint Aubin, 91192 Gif-sur-Yvette, France

composites and (ii) transition metal-incorporated carbon-nitrogen matrices (referred to as M-N-C, with M = Fe or Co) [7–9]. Recently, an extraordinary expectation towards the use of M-N-C catalysts for ORR electrocatalysis has grown, due to the recent and rapid progress in the field over the past 10 years, regarding improvement in the electrocatalytic activity, power performance, tolerance to CO, and, although more challenging, improvements in stability and durability as well, observed in both high and low pH conditions [10–14]. However, a better understanding of the nature and the number of the different active sites in pyrolyzed M-N-C materials and correlations with the ORR electrocatalysis at different pH values is still required for an optimized choice of such catalysts as a function of the operating conditions, in particular regarding the operating pH of the fuel cell device.

When the pH changes from acidic (PEMFC, pH~1) to alkaline (AEMFC, pH~13) conditions, the overall four-electron O_2 reduction changes from $O_2 + 4H^+ + 4\ e^- \rightarrow 2\ H_2O$ to $O_2 + 2\ H_2O + 4\ e^- \rightarrow 4\ OH^-$, in acid and alkaline conditions, respectively, with implications on the mechanism, selectivity, and intrinsic activity of different catalytic sites. The ORR mechanism can also proceed indirectly, first involving 2 electrons leading to H_2O_2 or HO_2^- peroxide intermediate release ($O_2 + 2\ H^+ + 2e^- \rightarrow H_2O_2$ and $O_2 + H_2O + 2e^- \rightarrow HO_2^- + OH^-$) followed by a second sequential 2-electron transfer, whereby H_2O_2 or HO_2^- is reduced to H_2O or OH^-, at the same or at a different active site ($H_2O_2 + 2\ H^+ + 2e^- \rightarrow 2\ H_2O$ and $HO_2^- + H_2O + 2\ e^- \rightarrow 3\ OH^-$). Chemical disproportionation of H_2O_2 and HO_2^- may also be considered in both media [1, 15]. In addition to the different roles of H^+ and OH^- species and different intermediate species in the two different electrolytes, the pH difference can also modify the double-layer structure, resulting in different possibilities of electron transfer mechanisms: inner- and outer-sphere [16, 17].

Many studies have investigated the nature of the different ORR active sites in M-N-C catalysts [18–20], and three main types of active sites have been proposed: N_xC_y, M-N_xC_y, and M@N-C [7], where N_xC_y sites are nitrogen functional groups in a carbon matrix, M-N_xC_y are atomically dispersed nitrogen-bonded metal centers embedded in a N-doped carbon matrix, and M@N-C sites are nanoparticulated metallic centers surrounded by a N-doped carbon shell (itself free of M-N_xC_y sites). In tuning the intrinsic ORR activity of these structurally and chemically different active sites, another important parameter is the nature of the metal (M), with all works reported since the 1990s pointing to iron (Fe) and cobalt (Co) as universally leading to the most active PGM-free metals, regardless of the nature of the metal-based sites, M-N_xC_y or M@N-C [21–23].

Regarding Co-N-C catalysts, Co-N_xC_y moieties have been pointed as the main active centers that catalyze the ORR, either in alkaline or acidic conditions [24–26]. Meanwhile, Co@N-C sites have shown ORR activity, with the N-C matrix providing protection of the metallic core, that would otherwise be rapidly leached out in acidic medium [26]. Along the same lines, the high ORR activity of Fe-N-C catalysts has been clearly linked to the content of Fe-N_xC_y sites, especially in low pH conditions [7, 27]. However, it has been recently reported that Fe-N-C catalysts containing Fe@N-C core-shell structures (without Fe-N_xC_y moieties) also can exhibit good ORR activity, either in high or in low pH conditions [19, 28, 29]. In summary, it is well-established that optimized M-N-C catalysts can achieve high activities towards ORR electrocatalysis, sometimes approaching those of PGM-based materials. However, it is still unclear which are the truthful activities of M-N_xC_y and M@N-C sites, when the catalysts are used in different pH conditions.

Herein, we study the ORR electrocatalytic activity and mechanism of two M-N-C catalysts exclusively comprising metal as M-N_xC_y sites (Fe or Co), two other M-N-C catalysts exclusively comprising metal as M@N-C core-shell structures (Fe or Co), and one N-C baseline material synthesized similarly as the other four materials but without addition of Fe or Co precursor under both acidic and alkaline conditions. The catalysts were characterized by transmission electron microscopy (TEM) and X-ray absorption spectroscopy (XAS). Their electrochemical activity was evaluated in acidic (0.1 mol L^{-1} H_2SO_4) and alkaline (0.1 mol L^{-1} NaOH) conditions using rotating ring-disk electrode (R(R)DE). This study demonstrates that changing the pH from acidic to alkaline results in a switch of the ability of Ar-pyrolized M-N_xC_y and M@N-C sites to reduce O_2; while M-N_xC_y sites (Fe-N_xC_y > Co-N_xC_y) are most active in acidic conditions, M@N-C (Fe@N-C > Co@N-C) reach a higher mass activity (powder mass) in alkaline conditions.

Experimental section

Electrocatalyst synthesis

The electrocatalysts were synthesized using the method described by Zitolo et al. [24], in which the zinc(II) zeolitic imidazolate framework ZIF-8 (purchased from BASF, Basolite Z1200), metal(II) acetate (Fe or Co), and 1,10-phenanthroline were mixed via dry planetary ball milling in optimized ratio of 200 mg phenanthroline, 800 mg ZIF-8, and either 0.5 wt.% or 5.0 wt.% of metal (Fe or Co) to the overall mass of the three precursors. The dry mixed powder of the catalyst precursor was then heated under Ar flow with a ramp rate of 5 °C min^{-1} to 1050 °C, and held at that temperature for 1 h, at which point the split-hinge oven was opened and the quartz tube and boat quenched to room temperature while still flowing Ar. The amount of Fe or Co before pyrolysis was either 0 (for N-C), 0.5, or 5.0 wt.% in relation to the total mass of metal salt, phenanthroline, and ZIF-8. Due to about 2/3 mass loss of phenanthroline and ZIF-8 during the pyrolysis, the Fe or Co content after pyrolysis is circa three times higher

than in the catalyst precursor before pyrolysis. The catalysts are labeled as M_x, where M is Fe or Co and *x* is the wt.% metal in the catalyst precursor before pyrolysis, either 0.5 or 5.0. As a benchmark catalyst, Pt nanoparticles (40 wt.%) supported on graphitized carbon (TEC10EA40E) was utilized, purchased from Tanaka Kikinzoku Kogyo (TKK).

Preparation of inks and layers

Inks for the formation of PGM-free catalyst layers were prepared by dispersing the catalytic powders (10 mg) with a 5 wt.% Nafion solution (50 μL, Sigma-Aldrich), isopropanol (854 μL, Carl Roth), and ultrapure water (372 μL, Millipore, 18.2 MΩ cm), followed by ultrasonic homogenization, as described by Kumar et al. [30]. For the benchmark catalyst, the ink was prepared in a similar way, consisting of Pt/C powder (5 mg), 5 wt.% Nafion solution (54 μL), isopropanol (1446 μL), and ultrapure water (3600 μL). Then, the desired aliquot of each prepared ink was dropped onto glassy carbon disk substrate of the RDE or RRDE (0.196 cm^2 for both), followed by drying with hot air under controlled rotation speed. The total loadings were in the range of 0.1 to 0.8 mg_{powder} cm^{-2} for PGM-free catalysts and 20 $\mu g_{Pt/C}$ cm^{-2} (on RDE) or 10 $\mu g_{Pt/C}$ cm^{-2} (on RRDE) for the Pt/C benchmark catalyst.

Electrochemical measurements

Before any electrochemical experiment, the glassware, polytetrafluoroethylene (PTFE)–based materials, and electrodes were cleaned with a 50% v/v solution of H_2SO_4 (Merck, Suprapur 96 wt.%)/H_2O_2 (Carl Roth, 30% w/w) followed by rinsing in ultrapure water (MQ grade, 18.2 MΩ cm, 1–3 ppm TOC) and hot ultrapure water. All glassy carbon disks were polished with 3 and 1 μm diamond polishing paste (Presi). Fresh Ar-saturated electrolytes were prepared from NaOH (Alfa Aesar, 50% w/w aq. soln.), H_2SO_4, and ultrapure water to obtain an electrolyte concentration of 0.1 mol L^{-1}.

The electrochemical measurements were performed using three-electrode electrochemical cells with the temperature controlled at 25 °C. A glass cell was used for acid medium and PTFE cell for alkaline medium. A commercial reversible hydrogen electrode (RHE, Gaskatel GmbH) connected to the cell by Luggin capillary was used as the reference electrode. To filter the high-frequency electrical noise, a Pt-wire immersed in the electrolyte was connected to the reference electrode. In each electrolyte, the counter electrode was a carbon sheet and the working electrode was glassy carbon coated with the investigated catalyst, with loading varying depending whether RDE or RRDE measurements were performed, as described below.

RRDE or RDE measurements were performed with Autolab PGSTAT302N and PGSTAT12 potentiostat, respectively. For RDE measurements, a homemade glassy carbon cylinder (glassy carbon Sigradur® from Hochtemperatur-Werkstoffe GmbH) embedded in a PTFE cylinder, coupled to a commercial system for controlling the rotation rate (Origalys), was utilized as the working electrode. For RRDE measurements, a Pt-ring and a glassy carbon disk tip (Pine Research) embedded in a PTFE rod was used.

For both RDE and RRDE measurements, electrochemical break-in of the thin-film electrodes was performed by applying 50 cyclic voltammograms (CVs) between 0.0 and 1.0 V vs. RHE at 100 mV s^{-1} in Ar-saturated 0.1 mol L^{-1} H_2SO_4 or 0.1 mol L^{-1} NaOH. Then, the CVs of the thin films were recorded in the same conditions at 10 and 5 mV s^{-1}. The ORR polarization curves were recorded at 5 mV s^{-1} in O_2-saturated electrolyte at 1600 rpm. All measurements were dynamically corrected from ohmic drop.

The kinetic current density for ORR (i_k) was determined according to Koutecky Levich (Eq. 1):

$$i_k = -\frac{(i_L.i)}{(i_L - i)} \tag{1}$$

where i_L is the oxygen diffusion–limited current density at 0.2 V *vs*. RHE and *i* is the Faradaic current after ohmic drop correction and capacitive current subtraction.

Consequently, the mass activity (i_{MA}) was calculated using the equation below:

$$i_{MA} = \frac{i_k}{m} \tag{2}$$

where *m* is the catalyst mass on the glassy carbon electrode.

For RRDE measurements, the same initial steps as described for RDE measurements were followed. Additionally, the catalyst loading was 0.1 mg_{powder} cm^{-2} except for the Pt catalyst for which 10 μg_{Pt} cm^{-2} was utilized. To detect H_2O_2 or HO_2^- produced during ORR, the Pt-ring was polarized at 1.2 V vs. RHE. The peroxide quantification further requires the value of the collection efficiency (*N*), which was determined experimentally using the Fe^{3+}/Fe^{2+} redox couple from $K_3Fe(CN)_6$ salt, as described before [31]. The experimental value was found to be $N = 0.24$. The equations below were utilized for determining the number of electrons transferred along the ORR (n_{e-}, Eq. 3) and the peroxide percentage (Eq. 4):

$$n_{e^-} = \frac{4i_d}{i_d + \left(\frac{i_r}{N}\right)} \tag{3}$$

$$\%H_2O_2 \; or \; \%HO_2^- = \frac{2\frac{i_r}{N}}{\left(\frac{i_r}{N}\right) + i_d} \times 100 \tag{4}$$

where i_d and i_r are the currents at the disk and Pt-ring, respectively.

Physicochemical characterizations

TEM images of the electrocatalysts were recorded using a JEOL 2010 TEM instrument operated at 200 kV with a point-to-point resolution of 0.19 nm. Acquisition of Co and Fe *K*-edge X-ray absorption spectra were made at room temperature, in transmission mode at SAMBA beamline of the Synchrotron SOLEIL (Gif-sur-Yvette, France), with a focusing Si(220) monochromator. Pellets were prepared by mixing an adequate catalyst amount with PTFE powder so as to get an optimal absorption signal. The Athena software was employed for XAS data analysis, comprising the XANES (X-ray absorption near edge structure) spectra and the Fourier transforms of the EXAFS (extended X-ray absorption fine structures) signals [32].

Results and discussion

Detailed physicochemical characterization of the catalysts using XAS, Raman and ^{57}Fe Mössbauer spectroscopy, TEM, X-EDS, and XRD analyses [30, 33] have been presented in previous studies published by Zitolo et al. [33] and Kumar et al. [30]. In brief, the important observations previously reported are that the catalysts with 5 wt.% metal contents ($M_{5.0}$) comprise metallic or metal carbide nanoparticles surrounded by a shell of N-doped graphitic carbon (here referred to as M@N-C), while catalysts with low metal content ($M_{0.5}$) comprise metal cations that are atomically dispersed in the N-doped carbon matrix and coordinated by nitrogen atoms (here referred to as M-N_xC_y). Moreover, metal-based particles in the $Fe_{5.0}$ and $Co_{5.0}$ catalysts were found to be exclusively Fe_3C and metallic Co, respectively. Other important findings are related to the presence of more graphitic carbon structure in the neighborhood of the metal-based nanoparticles for $M_{5.0}$ catalysts, as well as the presence of smaller graphite crystallites in $M_{0.5}$.

Figure 1 displays physicochemical characterizations of $Fe_{0.5}$, $Fe_{5.0}$, $Co_{0.5}$, and $Co_{5.0}$. TEM images shown in Fig. 1(a)–(d) evidence that the synthesized catalysts exhibit two different carbon nanostructures: stacked graphitic layers (mainly for $Fe_{5.0}$ and $Co_{5.0}$) and sheet-like layers with poorly structured carbon, for both metal contents. This indicates that the initial highly structured and organized ZIF-8 carbon and nitrogen precursor was significantly modified during pyrolysis. As reported previously [26, 29], these results confirm that the catalysts present particular characteristics denoting the existence of two distinct zones: (i) in one case, the presence of segregated metallic-based nanoparticles (10–100 nm) is seen, as confirmed by the dark spots in the images of the higher metal load materials ($Fe_{5.0}$ and $Co_{5.0}$), and (ii) a zone containing the metals atomically dispersed over the carbon-nitrogen matrix ($Fe_{0.5}$ and $Co_{0.5}$).

Figure 1 (e) and (f) show XANES spectra for both types of catalysts at the Fe (energy = 7112 eV) and Co (energy = 7709 eV) *K*-edges, respectively, where reference spectra for Fe and Co foils and Fe_3C were included for comparison. The high similarities between the XANES signals obtained for $Fe_{5.0}$ and $Co_{5.0}$ with those shown for Fe_3C and metallic Co foils, respectively, clearly indicate that the black spots in Fig. 1 (b) and (d) for these samples are essentially zero-valent Fe and Co species [30]. In the cases of $Fe_{0.5}$ and $Co_{0.5}$, the shift towards higher energy of the edge with respect to that of the metal foil and the large hump peaking at ca. 20 eV above the energy of the metal edge is unequivocally evidencing that the Co and Fe atoms are present in oxidized states [24, 30, 33].

Fourier transforms of the EXAFS signals, either for the samples as well as for the metallic standards, are shown in Fig. 1 (g) and (h). First, it should be noted that the *x*-axis positions of the several peaks are related to the distance between the X-ray absorbing metal atoms and neighboring atoms present in the different coordination shells surrounding the element under investigation. However, the radial distances do not exactly correspond to the atomic distances, since a phase shift correction must be applied to precisely estimate the interatomic distance and this correction depends on the nature of the backscattering elements [33]. Here, in the case of the Fe-containing materials (Fig. 1(g)), the presence of the Fe-Fe coordination (peak next to 2.1–2.2 Å) is only detected for $Fe_{5.0}$, as concluded from comparisons with the features of the Fe_3C [34] and results reported by Zitolo et al. [33]. In this case, a weak shoulder is also observed at radial distance near to 1.6–1.7 Å, and this may be related to the existence of some Fe-C or Fe-N interatomic distances in the second coordination sphere, possibly assigned to Fe-C interatomic distance in Fe_3C or to Fe-C interatomic distance from a small amount of Fe-N_xC_y moieties. However, ^{57}Fe Mössbauer transmission spectra for the same material (catalyst named as $Fe_{5.0}$RP in that work) performed in our former work [30] revealed the presence of only one sextet component with Mössbauer parameters exactly matching those of Fe_3C. The ^{57}Fe Mössbauer spectra confirmed the conclusions drawn from XANES and EXAFS signals, and thus, it may be concluded that $Fe_{5.0}$ does not contain Fe-N bonds from Fe-N_xC_y moieties. This is also in line with the absence of EXAFS signal for $Fe_{5.0}$ at a radial distance of ca. 1.0 Å, typical for Fe-N distance in FeN_xC_y moieties. For the $Fe_{0.5}$ material, the main peak located at 1.4 Å and the less-intense peak at 2.4 Å might be assigned to Fe-N and Fe-C backscatterings, respectively [33]. It should also be noted that the signals for more distant shells are only clearly observed for the Fe foil, indicating the absence of long-distance ordered coordination shells in Fe-containing samples, particularly for $Fe_{0.5}$. This observation is in agreement with usual propositions that, for these kind of systems, metal species are atomically dispersed in the carbon-nitrogen matrix for $Fe_{0.5}$ and, mainly as Fe_3C for $Fe_{5.0}$. Finally, the EXAFS of the

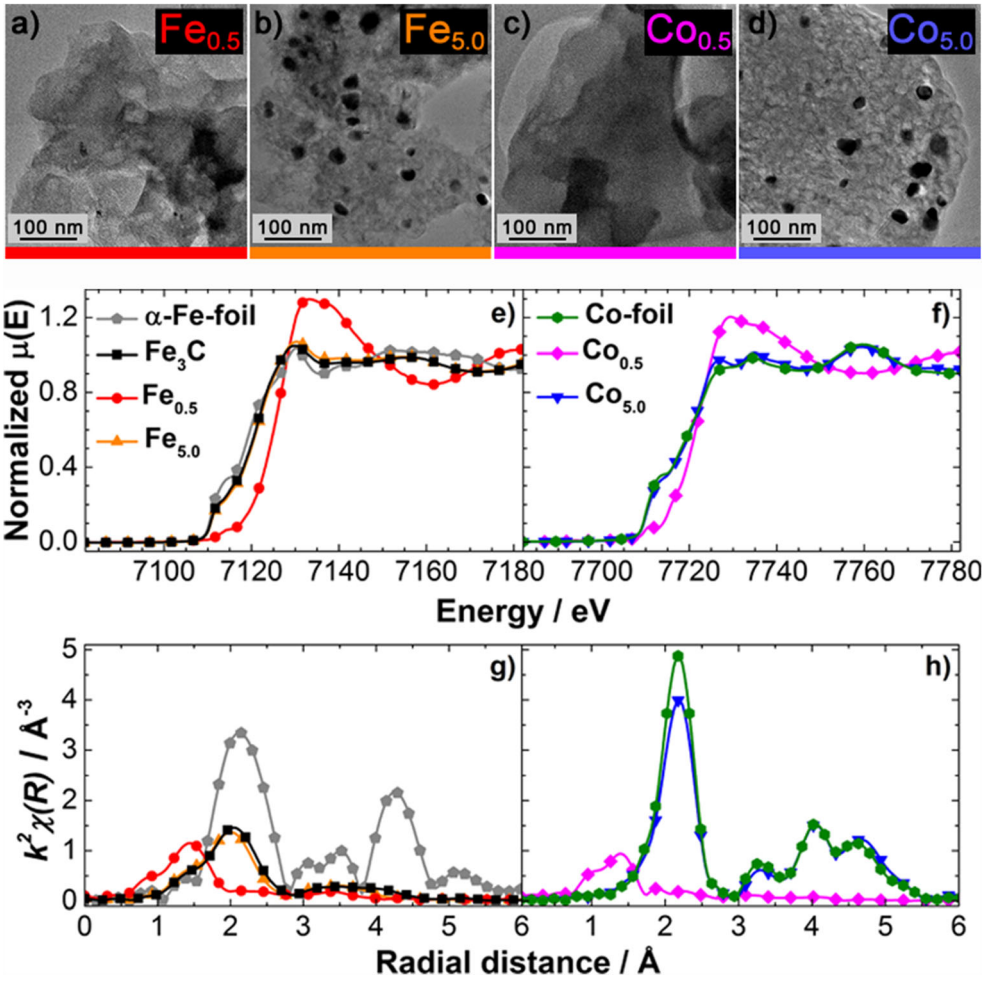

Fig. 1 Physical and chemical properties of metal-N_xC_y and metal@N-C catalysts. (a–d) Representative transmission electron microscopy images, (e, f) XANES, and (g, h) Fourier transforms of the EXAFS spectra measured at Co or Fe *K*-edge. Adapted from ref. [30] with permission from The American Chemical Society

Co-based catalysts evidence two main differences with respect to the Fe-based catalysts: (i) in the case of $Co_{5.0}$, the Co-Co coordination extends to much longer shells resembling that of the Co foil, confirming that metallic Co is present as a principal species; (ii) in the case of $Co_{0.5}$, the XANES is similar to that of $Fe_{0.5}$ and calculations of XANES spectra for different model sites showed that a good match could be obtained with either porphyrinic (CoN_4C_{12}) or defective porphyrinic structures (e.g., CoN_3C_{10}) [24].

Figure 2 (a) and (b) show ohmic-drop corrected CVs for all four catalysts at a fixed loading in the thin-film electrode in acid and alkaline electrolytes, respectively. Results for a Fe- and Co-free N-doped carbon prepared otherwise similarly (labeled M_0) are included for comparison. For the $M_{5.0}$ and M_0 catalysts and either in acid or alkaline electrolytes, the CV features are those typically found for large capacitance systems, so that the currents are mostly related to charge accumulation in the double layer (non-faradic and non-redox process) at the catalyst | electrolyte interface. This general trend differs in the case of $Fe_{0.5}$ in acid medium, for which a redox pair, consistent with the Fe^{3+}/Fe^{2+} couple, is apparent at ca. 0.7 V vs. RHE. Results in Fig. 2(a) also show that the CV profiles exhibit similar current intensities, except for the $Fe_{0.5}$ catalyst, for which the intensities are unequivocally higher than the others, which we relate to a larger carbon-specific surface area [30], and/or features associated to the presence of surface defects, as compared with the other cases. Another aspect is that $Co_{0.5}$ has a larger surface area than $Fe_{0.5}$ [30], yet results in a CV that is distinct from that of $Fe_{0.5}$ and more similar to those of the other catalysts with lower BET area. This may be explained by the presence of too narrow micropores in this case, which do not effectively contribute to the charge accumulation in the double layer, and/or to the more organized structure of the carbon phase, leading to a lower content of surface groups (N or O) and thereby decreased capacitive currents [35]. The absence of redox peak assigned to Co cations in $Co_{0.5}$ is explained by the fact that the $Co^{2+/}Co^{3+}$ redox in a similar Co-N-C catalyst (flash pyrolyzed) was found at potentials well above the upper limit of the CVs presented here [24]. However, we noticed anodic current at high potential values for $Co_{5.0}$ in alkaline electrolyte, which indicates that Co nanoparticles are progressively covered by a thin passivating layer of $Co(OH)_2$ followed by the oxidation of $Co(OH)_2$ to Co_2O_3 and CoOOH species, in agreement with the literature [36, 37].

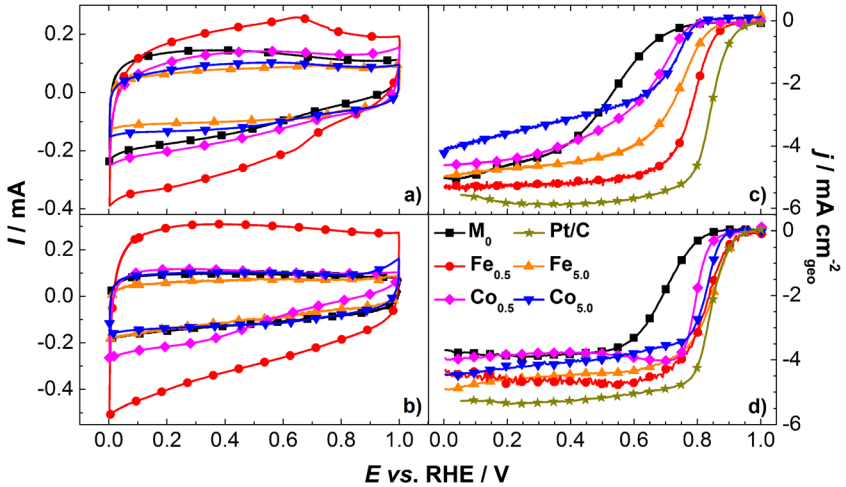

Fig. 2 Electrochemical properties of Fe-N-C and Co-N-C catalysts in alkaline and acid media. CVs in Ar-saturated electrolyte 0.1 mol L^{-1} (a) H_2SO_4 and (b) NaOH at 10 mV s^{-1}; ORR polarization curves in O_2-saturated electrolyte 0.1 mol L^{-1} (c) H_2SO_4 and (d) NaOH at 5 mV s^{-1} and 1600 rpm. For all measurements: 0.8 mg_{powder} cm^{-2} and 25 °C. For comparison, Pt/C (20 $\mu g_{Pt/C}$ cm^{-2}) and M_0 (N-C without Fe or Co) catalysts were utilized. Measurements were repeated at least three times leading to the same results (all results and errors are tabulated in the Supporting Information)

Finally, the absence of Fe redox features for the $Fe_{5.0}$ catalyst in acidic conditions is consistent with previous results showing that in this case all Fe is present as encapsulated metal carbide nanoparticles [30]. This implies that these species, even when present in the catalyst, have no direct contact with the electrolyte.

Polarization curves for the ORR were constructed by subtracting the capacitive currents of CV (at 5 mV s^{-1}) in Ar-saturated electrolytes from those related to the ORR, and employed to evaluate the ORR activity of the catalysts (M_0, $M_{0.5}$, and $M_{5.0}$). These results are shown in Fig. 2 (c) and (d), for the acid and alkaline electrolytes, respectively, while results obtained for a Pt/C catalyst were included for comparison. Generally, results show that all onset potentials are higher for Fe-N-C than for Co-N-C catalysts, denoting the higher activity of Fe-N-C materials for the ORR electrocatalysis. Following previous descriptors for the ORR activity on M-N-C catalysts, these differences in activity can be discussed in terms of the possibility that the reaction may occur involving inner- and outer-sphere electron transfer processes in alkaline media [16, 17], and also in terms of the binding energy of O_2 on M^{2+} active metal species in acid media [21], as detailed below.

In alkaline conditions, both outer- and inner-sphere electron transfer processes can co-exist in the same electrocatalyst at different potentials [16, 17]. At potentials > 0.8 V vs. RHE, the outer-sphere electron transfer is essentially inoperant and the reaction can occur by the direct adsorption of desolvated O_2 on the active sites, thus following the inner-sphere electron transfer [17]. In this case, the onset potential for the ORR is dependent on the binding energy between O_2 and the active metallic center (M^{2+}), which in turn is directly related to the M^{3+}/M^{2+} redox potential [17, 18, 21, 38]. Based on the fact that the redox potential of Co^{3+}/Co^{2+} ($E^o = 1.92$ V) is much higher than that of Fe^{3+}/Fe^{2+} ($E^o = 0.77$ V) [39], the O_2 molecule adsorbs much weakly and/or to a lesser extent on Co^{2+}, and in this way, the ORR onset potential for Co-N-C would be smaller than that for Fe-N-C catalysts, as observed in Fig. 2(d). In acidic conditions, inner-sphere electron transfer is the only possibility for the ORR electrocatalysis [16, 17]. Therefore, the causes of the differences in the ORR onset potentials on different metallic centers are explained similarly to the alkaline medium.

Figure 2 (c) shows that in acidic conditions, $Fe_{0.5}$ reaches the highest onset potential among all catalysts (0.92 ± 0.01 V), being only 0.04 V smaller than that of Pt/C (see details in the Supporting Information). The behavior of this catalyst confirms the high importance of having atomically dispersed Fe-N_xC_y active sites for allowing the occurrence of the Fe^{3+}/Fe^{2+} oxi-reduction process, as detected by CV. This couple seems to be the cause of the enhanced ORR electrocatalysis [40, 41] compared with the other catalysts. As already discussed in the literature [5, 17, 21], the active sites first generate Fe^{2+} from the reduction of Fe^{3+} (Eq. 5), which next promotes the displacement of adsorbed H_2O by O_2, accompanied by an electron transfer of Fe^{2+} to O_2 (Eq. 6); the $[Fe^{3+}$-$OH^-]_{ads}$ species would be regenerated in the following reaction step, so that the process becomes cyclically repeated:

$$\left[Fe^{3+}{-}OH^-\right]_{ads} + H^+ + e^- \rightleftharpoons \left[Fe^{2+}{-}OH_2\right]_{ads} \quad (5)$$

$$\left[Fe^{2+}{-}OH_2\right]_{ads} + O_2 \rightarrow \left[Fe^{3+}{-}O_2^-\right]_{ads} + H_2O \quad (6)$$

In acid media, other studies have shown that the onset potential for the ORR is directly related to the redox potential of the metal in the M-N_xC_y sites [17, 21, 28]. Here, such a redox process was only evident for $Fe_{0.5}$; it was not seen for

$Fe_{5.0}$ because in this case the only catalyst metal phase is formed by Fe_3C particles surrounded by a nitrogen-carbon shell (Fe@N-C). Finally, in the case of the Co-N-C catalysts in acid media, although results in Fig. 1 show that $Co_{0.5}$ presents the same atomic distribution as $Fe_{0.5}$, the corresponding CV does not evidence the occurrence of redox processes. This is because the presence of redox features of Co only appears at potentials well above the onset of the ORR, as is the case of Co^{3+}/Co^{2+}. From the results in Fig. 2(c), it is seen that the activity of the Co-N-C catalysts for the ORR is in fact not so much superior to that of M_0, which demonstrates the smaller role of Co-N_xC_y and Co@N-C for the promotion of the ORR electrocatalysis.

In alkaline medium, for the Fe-N-C catalysts (Fig. 2(d)), results show that the ORR onset potentials are very close (or equal, in the case of $Fe_{5.0}$) to those of Pt/C (0.97 ± 0.01 V), that is, 0.97 ± 0.01 V for $Fe_{5.0}$ and 0.95 ± 0.01 V for $Fe_{0.5}$. This high catalytic activity of $Fe_{5.0}$ evidences that in this medium, the Fe@N-C sites are active for the ORR, in contrast to the acid medium. Although substantially smaller than those of the Fe-N-C materials, the same catalytic phenomena are seen for the Co@N-C and Co-N_xC_y materials, for which the values of onset potential are 0.84 ± 0.01 V and 0.82 ± 0.01 V, respectively. In fact, a similar enhancement of catalytic activity is also seen in the absence of metallic centers (M_0). The higher activity of the Fe@N-C active sites in alkaline medium can be assigned to the enhancement of electrical conductivity of nitrogen-carbon and a synergistic effect between the metallic centers and the nitrogen-carbon shell. This is in line with recent results demonstrating that a higher degree of graphitization of carbon is beneficial to the electrical conductivity [42] and that synergies between the nitrogen-carbon shell and metallic centers contribute to efficient ORR electrocatalysis [19, 28, 43–46].

Another aspect to be discussed is the cause of the positive shift on the onset potential when the pH is changed from low to high values. This fact may be related to the OH_{ads} coverage and its desorption to regenerate the active metallic center M^{2+} [5, 18, 21]. Thus, a higher concentration of OH^- species in the electrolyte (alkaline media) seems to favor high coverages of OH_{ads}. In contrast, the effective OH_{ads} coverage in acidic conditions requires more energy due to the much smaller OH^- availability to generate and regenerate the M^{2+} active center, as shown above (Eqs. 5–6); also Fe^{3+} species can be poisoned by strong adsorption of H_2O, blocking the generation of Fe^{2+} species active for ORR [47].

Interestingly, the change in pH from acid to alkaline leads to a lower increase of the onset (half-wave) potentials by 30 mV (30 mV) for $Fe_{0.5}$ and 100 mV (70 mV) for $Fe_{5.0}$. This indicates that the activity of the Fe-N_xC_y sites in the present case is little affected by the pH, so that the $Fe_{0.5}$ catalyst can promote the ORR electrocatalysis with similar efficiency, either at high or at low H^+/OH^- concentrations. In contrast, results for Fe@N-C sites denote larger variations of onset/half-wave potentials, but the shift is smaller in the case of the half-wave potential, possibly indicating some occurrence of inner- and outer-sphere electron transfer mechanisms in alkaline medium, depending on the electrode potential. These behaviors were not found in Co-N-C catalysts, and, then this feature is exclusively related to Fe-N-C catalysts.

For the investigation of PGM-free catalyst loading effects on the mass activity for ORR electrocatalysis, the $Fe_{0.5}$ catalyst was selected in both pH conditions. Then, that catalyst loading effect was evaluated for $Fe_{0.5}$ in the range of 0.1 to 0.8 mg_{powder} cm^{-2} in 0.1 mol L^{-1} H_2SO_4 and 0.1 mol L^{-1} NaOH electrolytes, and the results are shown in Fig. 3. CV profiles in Fig. 3 (a) and (b) exhibit the expected proportional increase of the capacitive currents from low to high catalyst loadings in both pH conditions. For example, at 0.4 V, the capacitive currents increase linearly with the catalyst loading (see Fig. 1 – Supporting Information). This is mainly caused by the increase in the electrochemically available area, which is more pronounced in acidic conditions due to some contributions of currents related to redox processes of Fe^{3+}/Fe^{2+} and of oxygen functional groups present in the carbon matrix. As described in the literature [48], the oxidative process of carbon causes changes in the magnitude of the capacitive current at low pHs, while in alkaline media, the graphitic structures are less functionalized because they become hydrophilic enough for releasing some carbon functional groups.

In Fig. 3 (c) and (d), the results evidence a displacement of the ORR onset and half-wave potentials to higher values and increased oxygen diffusion–limited current densities (in the range of 0.0 V to 0.55 V) with the increase of the catalyst loading, with the effects being higher in the acid medium. This increase in the oxygen diffusion–limited current densities with the increase of the catalyst loading is probably related to the increased residence time of reactant/intermediate species [49, 50], like OH^-, O_2, H_2O_2, or HO_2^- inside the catalyst layer, enhancing their further reduction to complete the 4-electron process. Moreover, a sufficient number of active sites are necessary to catalyze the ORR efficiently [49, 50]; otherwise, no oxygen diffusion–limited currents appear, which in acid media seems to be the case for loadings ≤ 0.2 mg_{powder} cm^{-2}. In alkaline electrolytes, this effect may be minimized by the electrostatic interaction of anionic HO_2^- species with the Fe^{2+} cation from Fe-N_xC_y active sites [16, 17, 40], thus driving the ORR to OH^- even in thin catalyst layers (as also observed in Fig. 4) [51].

The oxygen diffusion–limited currents for the M-N-C catalysts are all smaller than those observed for Pt/C (Fig. 2(c–d)), that is known to lead to a predominant 4-electron ORR mechanism (O_2 is mostly reduced to H_2O in acid or OH^- in alkaline electrolytes). To discuss these issues, the percentages of H_2O_2/HO_2^- formation and the number of electrons involved in the ORR were obtained from rotating ring-disk

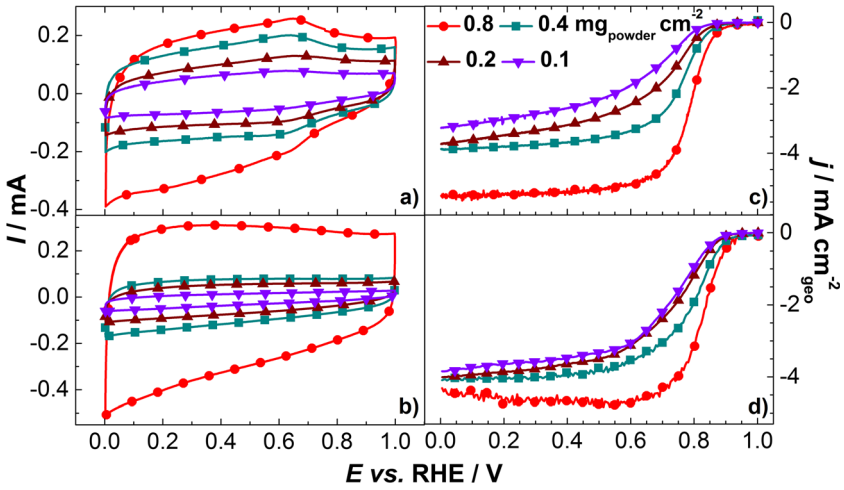

Fig. 3 Electrochemical properties of different $Fe_{0.5}$ catalyst loadings. CVs in Ar-saturated electrolyte 0.1 mol L^{-1} (a) H_2SO_4 and (b) NaOH at 10 mV s^{-1}; ORR polarization curves in O_2-saturated electrolyte 0.1 mol L^{-1} (c) H_2SO_4 and (d) NaOH at 5 mV s^{-1} and 1600 rpm. All measurements were performed at 25 °C. Measurements were repeated at least three times leading to the same results (all results and errors are tabulated in the Supporting Information)

measurements and these results are shown in Fig. 4. Generally speaking, the n_{e-} values for the M-N-C catalysts, and more specifically Fe-N-C, are not so different from those of Pt/C, either in acid or alkaline media, but this is more evident in the alkaline medium (see Tables 1 and 2 of the Supporting Information). Results related to the H_2O_2/HO_2^- formation are consistent with the above observations related to the number of transferred electrons in the ORR, as would be expected

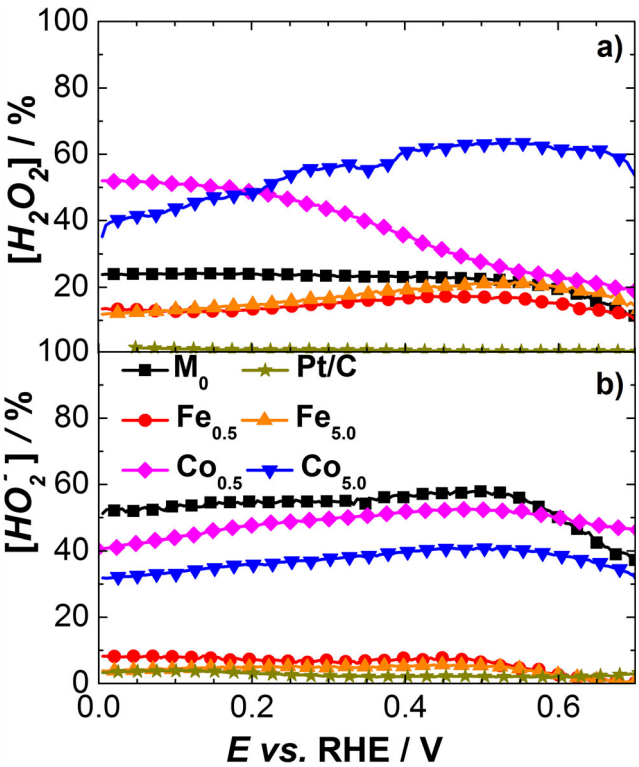

Fig. 4 RRDE measurements of Fe-N-C and Co-N-C catalysts. Peroxide percentage produced from ORR electrocatalysis in O_2-saturated electrolyte 0.1 mol L^{-1} (a) H_2SO_4 and (b) NaOH at 5 mV s^{-1} and 1600 rpm. For all measurements: 0.1 mg_{powder} cm^{-2} and 25 °C. For comparison, Pt/C (10 $\mu g_{Pt/C}$ cm^{-2}) and M_0 (without Fe or Co) catalysts were utilized (all results are tabulated in the Supporting Information)

because the same data and principles are used in the calculations of n_{e-} and $\%H_2O_2/HO_2^-$. These aspects regarding the number of electrons/percentages of H_2O_2/HO_2^- formation confirm that in the alkaline medium Fe-N_xC_y and Fe@N-C sites perform the reaction involving similar pathways and provide additional evidence that the Fe@N-C sites stabilize the HO_2^- intermediate as efficiently as Fe-N_xC_y. Therefore, synergistic effects in the Fe@N-C catalyst can provide an adequate energy binding between HO_2^- and the nitrogen-carbon shell, even without the direct contact between the Fe metallic center and the reactants or intermediates. In the cases of the Co-N-C materials, inferior n_{e-} values regularly ranging from 3 to 2 are observed in Fig. 4 and Tables 1 and 2 (Supporting Information).

Adequate adsorption energies of oxygenated intermediates species have been pointed to be essential for achieving high n_{e-} values in the ORR, and in this sense the anionic HO_2^- species formed along the ORR in alkaline conditions seems to be more strongly bound to the catalyst compared with the H_2O_2 species in acidic media, ensuring larger occurrence of the complete ORR electrocatalysis to OH^-. However, the higher amounts of H_2O_2/HO_2^- detected by the ring for the Co-catalysts, compared with the Fe-catalysts, may mean that the binding energies of H_2O_2/HO_2^- on Co-N_xC_y sites are small [21, 24, 52], as it would be also expected for the Co@N-C sites. In fact, trends observed here regarding the onset potentials, oxygen diffusion–limited currents, and number of electrons transferred in the ORR were similar to those observed in other studies of the ORR electrocatalysis in other Fe-N-C and Co-N-C catalysts [24, 53–55].

Further information about the reaction mechanism was obtained from Tafel plots constructed in the high-potential region of the ORR polarization curves and expressed in terms of the mass activity of the catalysts (i_{MA}), calculated as described in the "Experimental section." Results are shown in Fig. 5. The slopes of the resulting lines (Tafel slopes) were calculated, and the values are summarized in Tables 1-4 of the Supporting

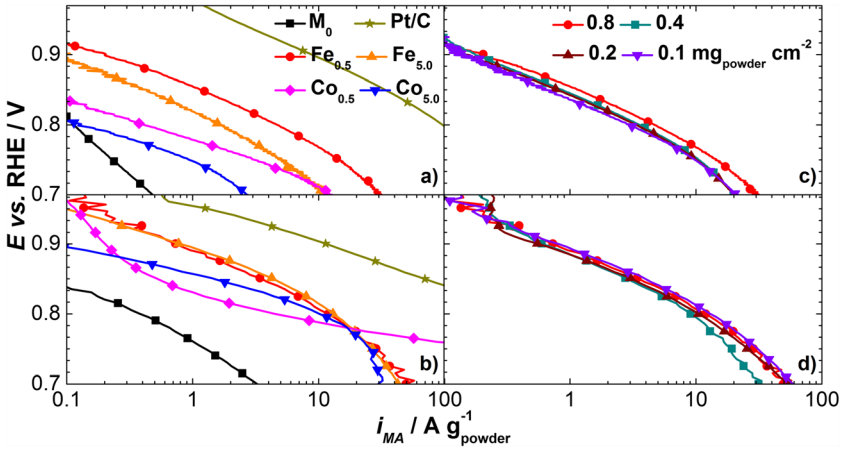

Fig. 5 Mass-transport-corrected Tafel plots of Fe-N-C and Co-N-C catalysts at fixed loading, and for $Fe_{0.5}$ on different catalyst loadings. Performed in O_2-saturated electrolyte 0.1 mol L^{-1} (a, c) H_2SO_4 and (b, d) NaOH at 5 mV s^{-1}, 1600 rpm, and 25 °C. For (a, b) measurements: 0.8 mg_{powder} cm^{-2}; Pt/C (10 $\mu g_{Pt/C}$ cm^{-2}) and M_0 (without Fe or Co) catalysts were utilized. Measurements were repeated at least three times leading to the same results (all results and errors are tabulated in the Supporting Information). In (c, d) panels, different $Fe_{0.5}$ loadings were used

Information (see Supporting Information). First, it is noted that $Fe_{0.5}$ and $Fe_{5.0}$ exhibit higher Tafel slopes as compared with $Co_{0.5}$ and $Co_{5.0}$ in both media (Fig. 5(a–b)), and this is consistent with the occurrence of distinct ORR mechanisms and/or rate-determining steps in the two classes of investigated materials. This observation is similar to those reported in published works when comparing Fe- vs. Co-based catalysts [22, 24, 53, 56].

The Tafel slopes for $Fe_{0.5}$ and $Fe_{5.0}$ catalysts are essentially the same in acid or alkaline media, demonstrating that the rate-determining step of the ORR mechanism may be the same in both cases, although involving different active sites and for $Fe_{0.5}$ in acid medium corresponding to a direct redox-mediated process. This implies that the different ORR activities seen for $Fe_{0.5}$ and $Fe_{5.0}$ in acid media (as evidenced for the different reaction overpotentials at a given mass activity) may be related to the different catalyst-specific active areas and/or different synergistic phenomena related to the different natures of the active centers. In alkaline media, since no redox features are detected but the activities are also close, one may conclude that the rate-determining step, the ORR mechanism, and eventually the specific active area are very similar for both catalysts. Finally, the results evidence the absence of mass-transport and conductivity problems related to the thickness/structure of catalytic layers, so that the magnitude of Tafel slopes is only related to the ORR mechanism [57].

For easier comparisons of the mass activity towards the ORR of materials, the previously calculated values at 0.85 V were plotted for each set of catalyst in both electrolytes (Fig. 6). Analyzing the results in acidic conditions (Fig. 6(a)), it is concluded that among all M-N-C catalysts, $Fe_{0.5}$ presents the highest mass activity for the ORR, followed by $Fe_{5.0}$, $Co_{0.5}$ and $Co_{5.0}$, as shown in Figs. 5(a) and 6(a). This superior activity of $Fe_{0.5}$ compared with that of $Fe_{5.0}$ indicates

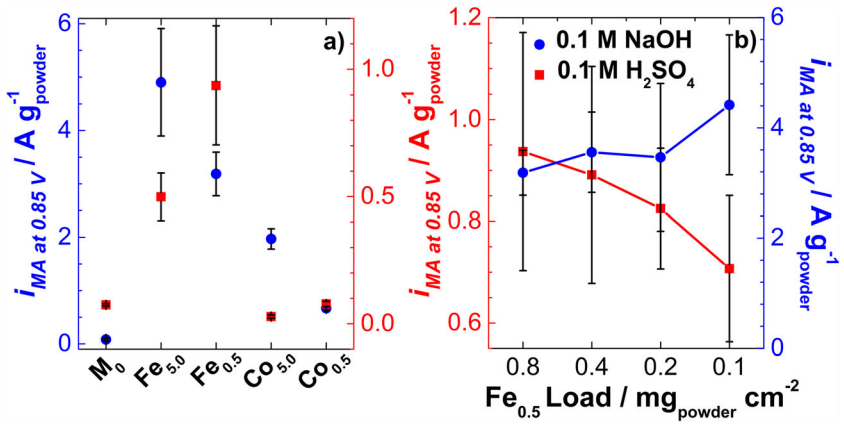

Fig. 6 Mass activity towards the ORR (i_{MA}) measured at 0.85 V for (a) all catalysts investigated in this study and (b) different $Fe_{0.5}$ catalyst loadings. All ORR experiments conducted at 1600 rpm, 5 mV s^{-1}, and 25 °C in O_2-saturated 0.1 mol L^{-1} (red) H_2SO_4 or (blue) NaOH electrolytes. Catalyst loadings of 0.8 mg_{powder} cm^{-2} were employed in (a). Measurements were repeated at least three times leading to the same results (all results and errors are tabulated in the Supporting Information)

a superior activity of Fe-N_xC_y sites compared with Fe@N-C; this trend is maintained for $Co_{0.5}$ with respect to $Co_{5.0}$. Therefore, we conclude that M-N_xC_y sites provide higher mass activity than M@N-C in acid conditions.

In alkaline solution, results show that $Fe_{5.0}$ presents the highest mass activity for the ORR, followed by $Fe_{0.5}$, $Co_{5.0}$, and $Co_{0.5}$. Therefore, generally speaking, it is seen that a high number of M@N-C sites (present in the catalysts with high metal content) can provide higher mass activity in alkaline medium as compared with a low number of M-N_xC_y sites, that is, predominant in catalysts with low metal content. These results show that, in alkaline media, the presence of atomically dispersed M-N_xC_y sites is not mandatory for the promotion of the ORR electrocatalysis with good efficiency. However, this mass activity distinction for materials containing M@N-C and M-N_xC_y sites seems to be evident only for Ar-pyrolyzed catalysts (or another inert gas). Indeed, recently, Santori et al. [58] have shown that other factors can lead to increased mass activity when switching from Ar- to NH_3-treated catalysts containing atomically dispersed Fe-N_xC_y sites. Further, another important aspect is that the catalyst without a metallic center (M_0) resulted in the poorest mass activity towards the ORR, stressing the crucial importance of having the metallic M@N-C or M-N_xC_y active sites for catalyzing the ORR, particularly in the case of iron. This is in agreement with the observation above reported, confirming that synergistic effects between the M^{2+} active metallic center and nitrogen-carbon shell (M@N-C) enhance the ORR mass activity, more than M-N_xC_y sites in high OH^- concentrations. Previous experimental studies provide support for the high activities found for Fe@N-C sites in alkaline media [10, 28, 44, 46, 59–61].

Figure 5 (c-d) and Figure 6 (b) allows discussing the mass activity as a function of the $Fe_{0.5}$ catalyst loading for the two pH conditions. It is first noted that the mass activities are higher in alkaline than those in acid media (except for 0.8 mg_{powder} cm^{-2}), following the same trends found in Fig. 6(a). Also, it is noted that there is an increase of the ORR mass activity with increased catalyst loading in acidic conditions, while the opposite occurs in alkaline media. These results confirm the need of longer residence time of reactants and/or intermediates inside the catalyst layer, as well as of the amount of Fe-N_xC_y sites in acid medium, while this is not the case in alkaline medium. These results have strong implications for the design of PGM-free catalysts layers in the cathodes of PEMFC and AEMFC.

Conclusions

In conclusion, we investigated the pH effect towards ORR electrocatalytic activities using a library of M-N-C catalysts featuring either M-N_xC_y or M@N-C active sites. The change in the pH of the electrolyte resulted in a switch of the ability of the active sites to reduce O_2; however, the higher performance for Fe-N-C compared with Co-N-C catalysts was maintained. Therefore, we reported there are two factors that alter the ORR activity: (i) the nature of the metallic center and (ii) the nature of the active sites. It is found that M-N_xC_y sites are more active when the ORR is performed in acidic conditions. For the most active center (Fe-N_xC_y), this property was assigned to the formation of Fe^{2+} from $Fe^{3+/}Fe^{2+}$ redox couple in direct contact with the electrolyte, reactants, OH_{ads}, and intermediates due to their adequate energy binding with the surface. Conversely, M@N-C presents better performance for ORR electrocatalysis in the alkaline conditions when normalized by powder mass. Fe@N-C led to the highest activity for Ar-pyrolyzed catalysts, displaying an effective synergistic effect between the iron as a metallic core with the nitrogen-carbon shells. It is emphasized that the indirect contact of the metallic center with surface hydroxyl and other intermediates drives the ORR electrocatalysis more effectively. Finally, Fe@N-C stabilizes HO_2^- intermediates adequately resulting in predominance of 4-electron transfer per oxygen molecule.

Acknowledgments The Synchrotron SOLEIL (Gif-sur Yvette, France) is acknowledged for provision of synchrotron radiation facilities at beamline SAMBA (Proposal No. 20171318). We also acknowledge Qingying Jia (Northeastern University, Boston, USA) for providing the EXAFS spectrum of Fe_3C.

Funding information This study was financially supported by the French National Research Agency through the CAT2CAT and ANIMA projects, the Coordenação de Aperfeiçoamento de Pessoal de Nível Superior (CAPES), Brazil (process number: 1614344), CAPES/COFECUB program (process numbers: 88887-187755/2018-00 and Ph-C 914/18), and the São Paulo State Research Foundation (FAPESP – process number: 2013/16930-7).

References

1. Shao M, Chang Q, Dodelet J-P, Chenitz R (2016) Recent advances in electrocatalysts for oxygen reduction reaction. Chem Rev 116(6): 3594–3657
2. Lopes T, Kucernak A, Malko D, Ticianelli EA (2016) Mechanistic insights into the oxygen reduction reaction on metal–N–C electrocatalysts under fuel cell conditions. ChemElectroChem 3: 1580–1590
3. Gasteiger HA, Kocha SS, Sompalli B, Wagner FT (2005) Activity benchmarks and requirements for Pt, Pt-alloy, and non-Pt oxygen reduction catalysts for PEMFCs. Appl Catal B Environ 56:9–35
4. Serov A, Zenyuk IV, Arges CG, Chatenet M (2018) Hot topics in alkaline exchange membrane fuel cells. J Power Sources 375:149–157
5. Li J, Alsudairi A, Ma ZF, Mukerjee S, Jia Q (2017) Asymmetric volcano trend in oxygen reduction activity of Pt and non-Pt catalysts: in situ identification of the site-blocking effect. J Am Chem Soc 139(4):1384–1387
6. Strateg Anal Inc. Mass Production Cost Estimation of Direct H_2 PEM Fuel Cell Systems for Transportation Applications : 2013

Update (2013) US Department of Energy, Washington. https://www.energy.gov/sites/prod/files/2014/11/f19/fcto_sa_2013_pemfc_transportation_cost_analysis.pdf .
7. Li J, Ghoshal S, Liang W et al (2016) Structural and mechanistic basis for the high activity of Fe-N-C catalysts toward oxygen reduction. Energy Environ Sci 9:2418–2432
8. do Rêgo UA, Lopes T, Bott-Neto JL et al (2019) Non-noble Fe-N_x/C electrocatalysts on tungsten carbides/N-doped carbons for the oxygen reduction reaction. Electrocatalysis 10:134–148
9. do Rêgo UA, Lopes T, Bott-Neto JL et al (2018) Oxygen reduction electrocatalysis on transition metal-nitrogen modified tungsten carbide nanomaterials. J Electroanal Chem 810:222–231
10. Zhong G, Wang H, Yu H, Peng F (2015) Nitrogen doped carbon nanotubes with encapsulated ferric carbide as excellent electrocatalyst for oxygen reduction reaction in acid and alkaline media. J Power Sources 286:495–503
11. Brocato S, Serov A, Atanassov P (2013) pH dependence of catalytic activity for ORR of the non-PGM catalyst derived from heat-treated Fe-phenanthroline. Electrochim Acta 87:361–365
12. Meng H, Jaouen F, Proietti E et al (2009) pH-effect on oxygen reduction activity of Fe-based electro-catalysts. Electrochem Commun 11:1986–1989
13. Elumeeva K, Ren J, Antonietti M, Fellinger TP (2015) High surface iron/cobalt-containing nitrogen-doped carbon aerogels as non-precious advanced electrocatalysts for oxygen reduction. ChemElectroChem 2:584–591
14. Rojas-Carbonell S, Artyushkova K, Serov A et al (2018) Effect of pH on the activity of platinum group metal-free catalysts in oxygen reduction reaction. ACS Catal 8:3041–3053
15. Ge X, Sumboja A, Wuu D et al (2015) Oxygen reduction in alkaline media: from mechanisms to recent advances of catalysts. ACS Catal 5:4643–4667
16. Ramaswamy N, Mukerjee S (2011) Influence of inner- and outer-sphere electron transfer mechanisms during electrocatalysis of oxygen reduction in alkaline media. J Phys Chem C 115:18015–18026
17. Ramaswamy N, Tylus U, Jia Q, Mukerjee S (2013) Activity descriptor identification for oxygen reduction on nonprecious electrocatalysts: linking surface science to coordination chemistry. J Am Chem Soc 135(41):15443–15449
18. Jia Q, Ramaswamy N, Hafiz H, Tylus U, Strickland K, Wu G, Barbiellini B, Bansil A, Holby EF, Zelenay P, Mukerjee S (2015) Experimental observation of redox-induced Fe-N switching behavior as a determinant role for oxygen reduction activity. ACS Nano 9(12):12496–12505
19. Zhong L, Frandsen C, Mørup S et al (2018) ^{57}Fe-Mössbauer spectroscopy and electrochemical activities of graphitic layer encapsulated iron electrocatalysts for the oxygen reduction reaction. Appl Catal B Environ 221:406–412
20. Singh SK, Takeyasu K, Nakamura J (2018) Active sites and mechanism of oxygen reduction reaction electrocatalysis on nitrogen-doped carbon materials. Adv Mater 1804297:1–17
21. Zagal JH, Koper MTM (2016) Reactivity descriptors for the activity of molecular MN_4 catalysts for the oxygen reduction reaction. Angew Chem Int Ed 55:14510–14521
22. Wu G, More KL, Johnston CM, Zelenay P (2011) High-performance electrocatalysts for oxygen reduction derived from polyaniline, iron, and cobalt. Science 332(80):443–447
23. Chen Z, Dodelet JP, Zhang J (eds) (2014) Non-noble metal fuel cell catalysts. Wiley, New York
24. Ranjbar-Sahraie N, Zitolo A, Fonda E et al (2017) Identification of catalytic sites in cobalt-nitrogen-carbon materials for the oxygen reduction reaction. Nat Commun 8:1–10
25. Subramanian P, Mohan R, Schechter A (2017) Unraveling the oxygen-reduction sites in graphitic-carbon Co–N–C-type electrocatalysts prepared by single-precursor pyrolysis. ChemCatChem 9:1969–1978
26. Perkas N, Schechter A, Gedanken A et al (2017) Electrochemical oxygen reduction activity of metal embedded nitrogen doped carbon nanostructures derived from pyrolysis of nitrogen-rich guanidinium salt. J Electrochem Soc 164:F781–F789
27. Dodelet JP, Chenitz R, Yang L, Lefèvre M (2014) A new catalytic site for the electroreduction of oxygen? ChemCatChem 6:1866–1867
28. Strickland K, Miner E, Jia Q et al (2015) Highly active oxygen reduction non-platinum group metal electrocatalyst without direct metal-nitrogen coordination. Nat Commun 6:1–8
29. Varnell JA, Tse ECM, Schulz CE et al (2016) Identification of carbon-encapsulated iron nanoparticles as active species in non-precious metal oxygen reduction catalysts. Nat Commun 7:1–9
30. Kumar K, Gairola P, Lions M, Ranjbar-Sahraie N et al (2018) Physical and chemical considerations for improving catalytic activity and stability of non-precious-metal oxygen reduction reaction catalysts. ACS Catal 8:11264–11276
31. Paulus UA, Schmidt TJ, Gasteiger HA, Behm RJ (2001) Oxygen reduction on a high-surface area Pt/Vulcan carbon catalyst: a thin-film rotating ring-disk electrode study. J Electroanal Chem 495:134–145
32. Ravel B, Newville M (2005) ATHENA, ARTEMIS, HEPHAESTUS: data analysis for X-ray absorption spectroscopy using IFEFFIT. J Synchrotron Radiat 12(Pt 4):537–541
33. Zitolo A, Goellner V, Armel V, Sougrati MT, Mineva T, Stievano L, Fonda E, Jaouen F (2015) Identification of catalytic sites for oxygen reduction in iron- and nitrogen-doped graphene materials. Nat Mater 14(9):937–942
34. Yuan K, Sfaelou S, Qiu M et al (2018) Synergetic contribution of boron and Fe-N_x species in porous carbons toward efficient electrocatalysts for oxygen reduction reaction. ACS Energy Lett 3:252–260
35. Raymundo-Piñero E, Kierzek K, Machnikowski J, Béguin F (2006) Relationship between the nanoporous texture of activated carbons and their capacitance properties in different electrolytes. Carbon 44:2498–2507
36. Cowling RD, Riddiford AC (1969) The anodic behaviour of cobalt in alkaline solutions. Electrochim Acta 14:981–989
37. Favaro M, Yang J, Nappini S, Magnano E, Toma FM, Crumlin EJ, Yano J, Sharp ID (2017) Understanding the oxygen evolution reaction mechanism on CoO_x using *operando* ambient-pressure X-ray photoelectron spectroscopy. J Am Chem Soc 139(26):8960–8970
38. Zúñiga C, Candia-Onfray C, Venegas R et al (2019) Elucidating the mechanism of the oxygen reduction reaction for pyrolyzed Fe-N-C catalysts in basic media. Electrochem Commun 102:78–82
39. Bard AJ, Faulkner LR (2001) Electrochemical methods: fundamentals and applications. Wiley, New York
40. Ramaswamy N, Mukerjee S (2012) Fundamental mechanistic understanding of zlectrocatalysis of oxygen reduction on Pt and non-Pt surfaces: acid versus alkaline media. Adv Phys Chem 2012:1–17
41. Tylus U, Jia Q, Strickland K et al (2014) Elucidating oxygen reduction active sites in pyrolyzed metal-nitrogen coordinated non-precious-metal electrocatalyst systems. J Phys Chem C 118:8999–9008
42. Pérez-Rodríguez S, Torres D, Lázaro MJ (2018) Effect of oxygen and structural properties on the electrical conductivity of powders of nanostructured carbon materials. Powder Technol 340:380–388
43. Deng D, Yu L, Chen X et al (2013) Iron encapsulated within pod-like carbon nanotubes for oxygen reduction reaction. Angew Chem Int Ed 52:371–375
44. Zhu J, Xiao M, Liu C et al (2015) Growth mechanism and active site probing of Fe_3C@N-doped carbon nanotubes/C catalysts: guidance for building highly efficient oxygen reduction electrocatalysts. J Mater Chem A 3:21451–21459

45. Watanabe M (1991) Design of alloy electrocatalysts for CO_2 reduction. J Electrochem Soc 138:3382
46. Hu Y, Jensen JO, Zhang W et al (2014) Hollow spheres of iron carbide nanoparticles encased in graphitic layers as oxygen reduction catalysts. Angew Chem Int Ed 53:3675–3679
47. Anderson AB, Sidik RA (2004) Oxygen electroreduction on Fe^{II} and Fe^{III} coordinated to N_4 chelates. Reversible potentials for the intermediate steps from quantum theory. J Phys Chem B 108:5031–5035
48. Yi Y, Weinberg G, Prenzel M et al (2017) Electrochemical corrosion of a glassy carbon electrode. Catal Today 295:32–40
49. Freitas KS, Concha BM, Ticianelli EA, Chatenet M (2011) Mass transport effects in the borohydride oxidation reaction - influence of the residence time on the reaction onset and faradaic efficiency. Catal Today 170:110–119
50. Schneider A, Colmenares L, Seidel YE, Jusys Z, Wickman B, Kasemo B, Behm RJ (2008) Transport effects in the oxygen reduction reaction on nanostructured, planar glassy carbon supported Pt/GC model electrodes. Phys Chem Chem Phys 10(14):1931–1943
51. Serov A, Artyushkova K, Andersen NI et al (2015) Original mechanochemical synthesis of non-platinum group metals oxygen reduction reaction catalysts assisted by sacrificial support method. Electrochim Acta 179:154–160
52. Goellner V, Armel V, Zitolo A et al (2015) Degradation by hydrogen peroxide of metal-nitrogen-carbon catalysts for oxygen reduction. J Electrochem Soc 162:H403–H414
53. Osmieri L, Monteverde Videla AHA, Armandi M, Specchia S (2016) Influence of different transition metals on the properties of Me–N–C (Me = Fe, Co, Cu, Zn) catalysts synthesized using SBA-15 as tubular nano-silica reactor for oxygen reduction reaction. Int J Hydrog Energy 41:22570–22588
54. Osmieri L, Monteverde Videla AHA, Ocón P, Specchia S (2017) Kinetics of oxygen electroreduction on Me-N-C (Me = Fe, Co, Cu) catalysts in acidic medium: insights on the effect of the transition metal. J Phys Chem C 121:17796–17817
55. Chen R, Li H, Chu D, Wang G (2009) Unraveling oxygen reduction reaction mechanisms on carbon-supported Fe-phthalocyanine and Co-phthalocyanine catalysts in alkaline solutions. J Phys Chem C 113:20689–20697
56. Goenaga GA, Roy AL, Cantillo NM et al (2018) A family of platinum group metal-free catalysts for oxygen reduction in alkaline media. J Power Sources 395:148–157
57. Chlistunoff J (2011) RRDE and voltammetric study of ORR on pyrolyzed Fe/polyaniline catalyst. On the origins of variable Tafel slopes. J Phys Chem C 115:6496–6507
58. Santori PG, Speck FD, Li J et al (2019) Effect of pyrolysis atmosphere and electrolyte pH on the oxygen reduction activity, stability and spectroscopic signature of FeN_x moieties in Fe-N-C catalysts. J Electrochem Soc 166:F3311–F3320
59. Lee JS, Park GS, Kim ST et al (2013) A highly efficient electrocatalyst for the oxygen reduction reaction: N-doped Ketjenblack incorporated into Fe/Fe_3C-functionalized melamine foam. Angew Chem Int Ed 52:1026–1030
60. Kim JH, Sa YJ, Jeong HY, Joo SH (2017) Roles of $Fe–N_x$ and $Fe–Fe_3C$@C species in Fe–N/C electrocatalysts for oxygen reduction reaction. ACS Appl Mater Interfaces 9(11):9567–9575
61. Gokhale R, Chen Y, Serov A et al (2016) Direct synthesis of platinum group metal-free Fe-N-C catalyst for oxygen reduction reaction in alkaline media. Electrochem Commun 72:140–143